metals

MDPI

Article

Reduction Behaviors of Silicon–Ferrite from Calcium and Aluminum in a Hydrogen-Rich Blast Furnace

Keshuai Du, Changqing Hu *, Xuefeng Shi and Guangqing Yang

College of Metallurgy and Energy, North China University of Science and Technology, Tangshan 063210, China; dukeshuai2022@163.com (K.D.); shixuefeng_0808@163.com (X.S.); yangguangqing@ncst.edu.cn (G.Y.)
* Correspondence: hiq-73@163.com

Abstract: Silicon–ferrite from calcium and aluminum (SFCA) is one of the primary binding phases in sinter. To better investigate the reduction process of SFCA under hydrogen-rich conditions in a blast furnace, isothermal reduction experiments were designed using three different hydrogen volume fractions (6%, 10%, and 14%) at temperatures within the blast furnace's lump zone range (1073 K, 1173 K, and 1273 K). The experimental results revealed that the reduction of SFCA proceeds in two stages: in the first stage, SFCA is initially reduced to Fe_3O_4; in the second stage, Fe_3O_4 is further reduced to FeO, with the equilibrium phases being FeO, $Ca_2Al_2SiO_7$, and Ca_2SiO_4. The fastest reduction rate was observed at 1273 K. When the hydrogen volume fraction was 6% and the temperatures were 1073 K, 1173 K, and 1273 K, the reaction mechanism followed the 3D diffusion model (G-B), with an apparent activation energy of 32.087 $kJ \cdot mol^{-1}$ and a pre-exponential factor of 0.1419. In comparison, at hydrogen volume fractions of 10% and 14%, the reaction mechanism shifted to the Shrinking core model (n = 3). The findings of this study can provide guidance for actual production and optimization of blast furnace parameters aimed at achieving low-carbon emissions in the steel-making process.

Keywords: hydrogen-rich blast furnace; SFCA; reductive behavior; phase evolution; reaction kinetic

Citation: Du, K.; Hu, C.; Shi, X.; Yang, G. Reduction Behaviors of Silicon–Ferrite from Calcium and Aluminum in a Hydrogen-Rich Blast Furnace. *Metals* **2024**, *14*, 1306. https://doi.org/10.3390/met14111306

Received: 7 October 2024
Revised: 14 November 2024
Accepted: 16 November 2024
Published: 19 November 2024

1. Introduction

To mitigate global warming, the steel industry must significantly reduce its CO_2 emissions [1–3]. The technology of blast furnace smelting with hydrogen-rich gases presents an effective pathway for achieving energy conservation and emission reduction in the steel industry. Techniques such as injecting coke oven gas, natural gas, and other hydrogen-rich gases into blast furnaces lead to an increased H_2 content in the gas within the furnace belly, thereby reducing the consumption of coal/coke and decreasing CO_2 emissions [4–7]. Sinter, serving as a crucial raw material for blast furnace ironmaking, primarily consists of hematite, magnetite, calcium ferrite, and slag phase. The quaternary system calcium ferrite of low Fe and high Al type constituted by CaO-Fe_2O_3-Al_2O_3-SiO_2 is one of the principal bonding phases of sinter, namely SFCA (silicon–ferrite of calcium and aluminum) [8]. SFCA possesses notable properties, including superior reducibility, high hardness, and a diminished low-temperature reduction disintegration rate [9,10]. A rigorous exploration of the carbon–hydrogen reduction mechanisms of SFCA is pivotal for advancing energy-efficient and emission-mitigating technologies, thereby bolstering productivity in the steel sector [11,12].

Researchers [13–17] have conducted extensive studies on the carbon–hydrogen reduction mechanisms of sinter, hematite, magnetite, as well as binary and ternary system calcium ferrites. For instance, Xudong Mao et al. [18] conducted isothermal reduction experiments and discovered that within the temperature range of 1023–1273 K, the reduction rate of hematite gradually accelerates with an increase in H_2 content in conjunction with kinetic models. Schurmann et al. [19] investigated the phase equilibrium and reduction

pathways of $CaO{\cdot}Fe_2O_3$ (CF) and $2CaO{\cdot}Fe_2O_3$ (C_2F) in a CO/CO_2 mixed gas atmosphere at 1273 K, thereby elucidating the reduction mechanism of binary system calcium ferrite. Senwei Xuan et al. [20] conducted isothermal thermogravimetric experiments to investigate the reduction kinetics of ternary calcium ferrite composed of $CaO\text{-}Fe_2O_3\text{-}Al_2O_3$. They calculated various reduction kinetic parameters of the samples, including the reduction extent, rate, activation energy, and model function. However, research on the carbon–hydrogen reduction mechanisms of quaternary system complex ferrite, particularly the reduction process of SFCA through the injection of hydrogen-rich gases under actual blast furnace conditions, is currently limited and merits further academic scrutiny.

Here, the hydrogen-rich reduction behavior of SFCA within the temperature range encountered in the lump zone of blast furnaces (1073–1273 K) was investigated. The research encompasses the following aspects: analyzing the phase transformations and microstructural evolution of SFCA during the reduction process at 1273 K; exploring the influence of varying temperatures and H_2 concentrations on the reduction behavior of SFCA using commonly employed gas–solid reaction kinetic models. The findings of our study can provide experimental data and theoretical guidance for practical production and the optimization of blast furnace parameters.

2. Experimental

2.1. Preparation of SFCA

The muffle furnace selected for this study is illustrated in Figure 1a, while the schematic diagram for the sintering of SFCA is shown in Figure 1b. The muffle furnace, model HLX-7-17, with a capacity of 18.4 L, was manufactured by Luo Yang Heng Lukiln Co., Ltd. (Luoyang, China) The heating element adopts silicon–molybdenum rods, which are arranged on all sides. Additionally, a quartz tube is positioned above the muffle furnace to facilitate external connections, and the atmosphere used during the firing process is air. All samples in the experiment were prepared via solid-state reaction methods, utilizing analytical reagents of Fe_2O_3, CaO, SiO_2, and Al_2O_3 as the experimental raw materials. Firstly, 100 g of experimental raw materials were weighed and placed into a corundum crucible. The experimental raw materials were mixed in accordance with the stoichiometric ratio corresponding to the SFCA chemical formula $Ca_5Si_2(FeAl)_{18}O_{36}$ (PDF 33-250), wherein Fe_2O_3 comprised 71.83%, CaO accounted for 17.72%, SiO_2 made up 6.73%, and Al_2O_3 constituted 5.72% of the total. Subsequently, the experimental raw materials were placed into an agate mortar and thoroughly ground to a fine powder, ensuring uniform mixing and compaction. Finally, the compacted samples were then positioned inside a muffle furnace and sintered at a temperature of 1553 K for a duration of 12 h. After the completion of the sintering process, the samples were allowed to cool down to room temperature under ambient conditions.

After calcination, the samples were crushed and sieved to obtain experimental specimens with a particle size range of 10.0–12.5 mm for subsequent isothermal reduction experiments. A portion of these samples was ground to a particle size smaller than 200 mesh (0.074 mm) for X-ray diffraction (XRD) analysis to determine the composition of SFCA. The XRD measurements were conducted using a Bruker D8 Advance diffractometer (operated at 40 kV × 400 mA), manufactured by Bruker Corporation, Ettlingen, Germany. A graphite monochromator was employed, with Cu Kα serving as the diffraction source. The analysis was performed in continuous scanning mode, with a step size of 0.02, a scanning speed of $10°{\cdot}min^{-1}$, and a scanning range of 10–90°. Another portion of samples was polished for scanning electron microscopy with energy-dispersive spectroscopy (SEM-EDS) analysis to investigate the distribution of major elements in the samples through area scanning. SEMs were carried out using a Phenom Pharos instrument from Eindhoven, The Netherlands, operated at an accelerating voltage of 15 kV. EDS was performed on the same instrument.

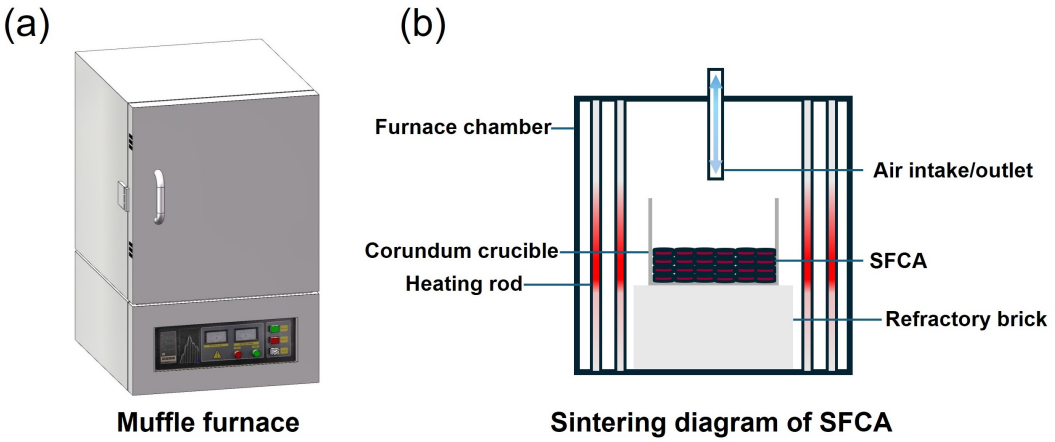

Figure 1. (**a**) Muffle furnace. (**b**) Sintering diagram of SFCA.

2.2. Isothermal Reduction Experiment

This paper primarily investigates the hydrogen-rich reduction behavior of SFCA within the temperature range of the blast furnace's lump zone. The lumpy zone of the blast furnace serves as the primary region for indirect reduction reactions, characterized by temperatures ranging from 873 to 1273 K. However, the practical reaction temperature range under experimental conditions necessitates consideration of the reaction rate; at excessively low temperatures, the reaction proceeds slowly. Consequently, the reduction temperature was set within this range (1073–1273 K). Based on a comprehensive consideration of ore reduction behavior and blast furnace operating parameters under hydrogen-rich smelting conditions in blast furnaces, this study refers to the simulation research on blast furnace gas composition conducted by Barrett et al. [21]. Consequently, reducing atmospheres with H_2 content levels of 6%, 10%, and 14% are selected for experimentation. The experimental atmosphere schemes are detailed in Table 1. Specifically, the simulated gas compositions with 6% and 14% H_2 content represent the base case (conventional blast furnace operation) and the maximum H_2 injection scenario, respectively. During the reduction process, the loss in weight is attributed to the extraction of O elements from iron oxides by CO and H_2. Hence, the ratio of the weight loss of the SFCA sample at a specific moment to the maximum weight loss achieved at the end of the reduction is defined as the conversion rate α. The detailed formula for calculating α is as follows:

$$\alpha = \frac{m_0 - m_t}{m_0 - m_1} \quad (1)$$

In Equation (1), m_0 represents the initial mass of the SFCA sample (g), m_t denotes the mass of the sample (g) at time t during the reduction process, and m_1 signifies the mass of the sample (g) after the reaction has completed.

Table 1. Experimental atmosphere scheme, w%.

Number	H_2	CO	CO_2	N_2
1	6	20	20	54
2	10	20	20	50
3	14	20	20	46

The isothermal reduction experiment was conducted in a tube furnace equipped with a balance. The equipment connection diagram is illustrated in Figure 2a, and the experimental schematic diagram is shown in Figure 2b. Firstly, 100 g of sample was weighed using an electronic balance (KT-C4Z, Ketan Zhengzhou and Equipment Co., Ltd., Zhengzhou, China) and placed into a hanging basket. The basket was then suspended in the isothermal zone of a tube furnace (HLG-8-17, Luo Yang Heng Lukiln Co., Ltd.,

Luoyang, China). The temperature was subsequently increased by adjusting the reduction temperature control program at a rate of 10 K·min^{-1}. During the initial heating process, a flow of N_2 at 5 L·min^{-1} was used for protection to purge the air from the tube furnace, thereby preventing reoxidation by CO and H_2 from affecting the experimental results. When the target temperature is reached, a mixed gas with a total flow rate of 10 L·min^{-1} was introduced to initiate the reduction process, which was conducted for a duration of 2 h. After the reduction experiment was completed, the flow of mixed gas was stopped, and instead, N_2 at 5 L·min^{-1} was introduced to cool the reduced sample down to room temperature. The programmed cooling rate of the tube furnace is 10 K·min^{-1}. After the reduction process was completed, one portion of the reduced sample was crushed and ground to a particle size of less than 200 mesh (0.074 mm) for XRD analysis. The other portion of the samples was polished for SEM-EDS testing, where the distribution of major elements within the sample was analyzed through point scanning.

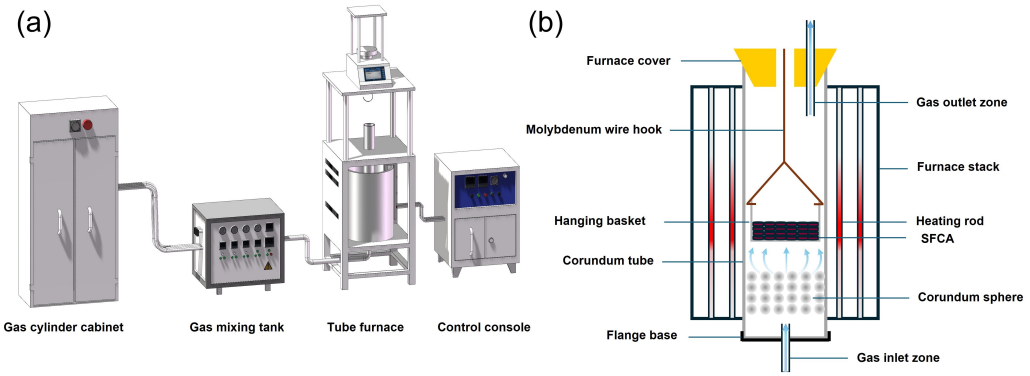

Figure 2. (**a**) Equipment connection diagram. (**b**) Experimental schematic diagram.

3. Results and Discussion

3.1. Characterization of SFCA Samples

The phase analysis of XRD is presented in Figure 3a. The XRD results of the synthesized SFCA phase perfectly agree with the corresponding standard card (PDF 33-250). Minor amounts of Fe_2O_3 phase are present in the sample at 2θ angles of 24, 33, 35, and 39°. To further ascertain the sample composition, the Rietveld full spectrum fitting method was employed in Figure 3b to perform structural refinement and quantification of the SFCA and Fe_2O_3 phases within the sample. As evident from the figure, the experimental values exhibit good agreement with the calculated values, confidence factor χ^2 of 2.25 and an R_{wp} of 12.8%. The refinement results indicate that the SFCA phase constitutes 99.67% of the sample, while the Fe_2O_3 phase accounts for 0.33%. The results of the SEM-EDS analysis, as depicted in Figure 4. It can be seen that all elements are uniformly distributed in the sample, and the atomic concentration and mass concentration of elements are basically consistent with the SFCA chemical formula $Ca_5Si_2(FeAl)_{18}O_{36}$, which further confirms the homogeneous chemical composition of the synthesized SFCA phase. In summary, a satisfactory SFCA sample was obtained and subsequently utilized for the reduction experiments.

3.2. Reduction Process of SFCA in Hydrogen-Rich Blast Furnace

To investigate the reduction process of SFCA under hydrogen-rich conditions, the variation curves of weight and conversion rate were plotted at a reduction temperature of 1273 K and an H_2 volume fraction of 6%. As shown in Figure 5, after 50 min of reduction, the weight of SFCA decreased from 100 g to 93 g, with a corresponding conversion rate of 100%, indicating the completion of the reduction process and the attainment of phase equilibrium. The conversion rates at reduction times of 3 min, 7 min, 12 min, and 50 min were 20%, 40%, 60%, and 100%, respectively. Therefore, detailed studies were conducted on the XRD and SEM-EDS of SFCA samples at these specific time points to investigate the hydrogen-rich reduction process of the samples.

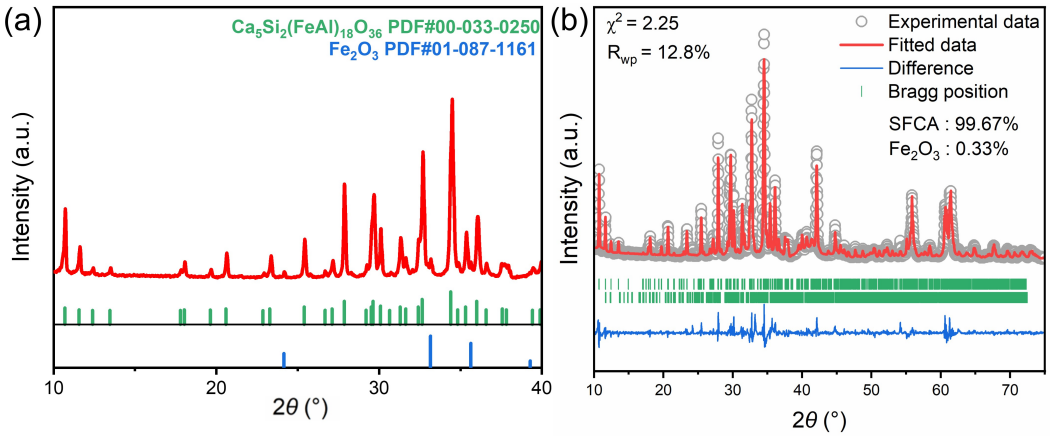

Figure 3. (**a**) XRD pattern of SFCA; (**b**) the Rietveld full spectrum fitting method.

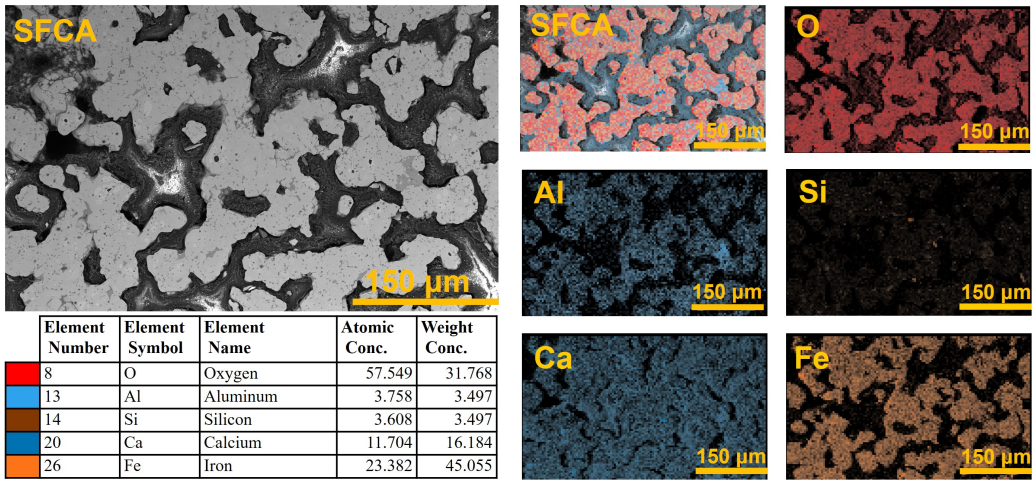

Element Number	Element Symbol	Element Name	Atomic Conc.	Weight Conc.
8	O	Oxygen	57.549	31.768
13	Al	Aluminum	3.758	3.497
14	Si	Silicon	3.608	3.497
20	Ca	Calcium	11.704	16.184
26	Fe	Iron	23.382	45.055

Figure 4. SEM and EDS of SFCA.

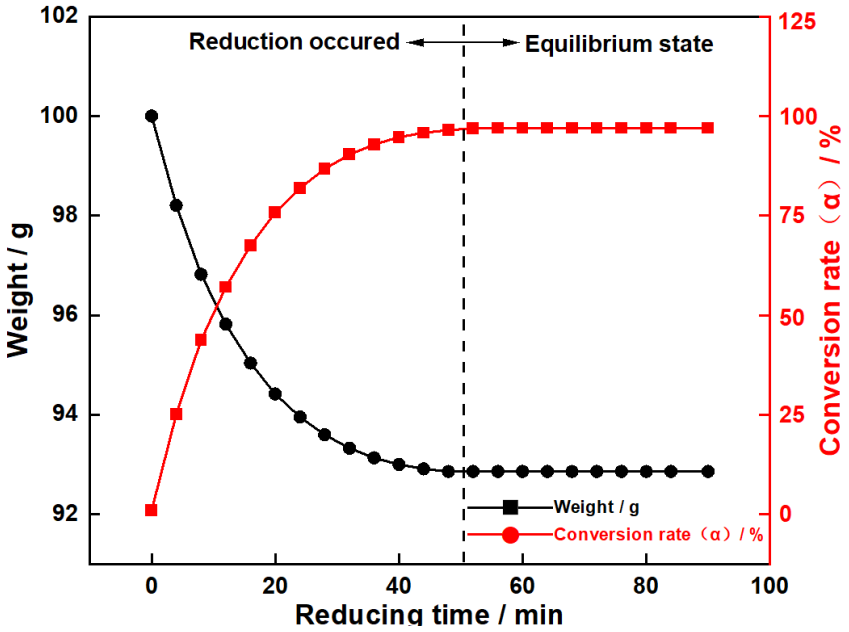

Figure 5. Weight and conversion rate as a function of reduction time at a H_2 volume fraction of 6%.

3.2.1. XRD Analysis of SFCA in the Reduction Process

The phase analysis results obtained by XRD are presented in Figure 6. As the reduction time and conversion rate increase, SFCA is ultimately reduced to wüstite (FeO), gehlenite ($Ca_2Al_2SiO_7$), and dicalcium silicate (Ca_2SiO_4). Figure 6a presents the XRD patterns of SFCA at various conversion rates. At a conversion rate of 20%, the primary constituents of the reduced products are SFCA and Fe_3O_4. As the conversion rate increases to 40%, the mineral composition still includes SFCA and Fe_3O_4, while FeO and $Ca_2Al_2SiO_7$ begin to form. When the conversion rate reaches 60%, the major components of the reduced products become Fe_3O_4, FeO, $Ca_2Al_2SiO_7$, and Ca_2SiO_4. At a 100% conversion rate, with the increase in reduction time, the degree of reduction remains essentially unchanged, and the final reduction stage is dominated by FeO, $Ca_2Al_2SiO_7$, and Ca_2SiO_4. To visually illustrate the reduction process of the reaction, Figure 6b employs kinetic analysis of XRD patterns. At a conversion rate of 0% and a 2θ angle of 34°, the main diffraction peak corresponds to the (240) diffraction line of SFCA. As the reduction reaction proceeds, the main diffraction peak gradually shifts from the (240) diffraction line of SFCA to the (311) diffraction line of Fe_3O_4. When the conversion rate exceeds 40%, the intensity of the diffraction peak for the Fe_3O_4 (311) diffraction line gradually weakens, while the intensities of the FeO (111) and FeO (200) diffraction lines start to increase, with the FeO (200) diffraction line eventually becoming the dominant diffraction peak. At a conversion rate of 60%, the FeO (220) diffraction line begins to form. Additionally, the Rietveld method for structural refinement and quantitative analysis is utilized to determine the relative content of each substance at different conversion rates. As depicted in Figure 6c, with an increasing conversion rate, the SFCA content decreases, while the Fe_3O_4 content shows an initial increase followed by a decrease. When the conversion rate surpasses 40%, the contents of FeO, $Ca_2Al_2SiO_7$, and Ca_2SiO_4 increase, and the variation trend of the main phases aligns with the kinetic analysis of XRD patterns shown in Figure 6b. From these XRD results, the reduction process of SFCA can be divided into two stages, as illustrated in Figure 6d. In the first stage, SFCA is reduced to form Fe_3O_4; in the second stage, Fe_3O_4 is further reduced to FeO.

During the reduction process, no other iron-containing phases are observed, possibly because the reaction between Al_2O_3 and CaO is more favorable, leading to the consumption of a significant amount of CaO with the appearance of $Ca_2Al_2SiO_7$ [9], thereby inhibiting the formation of other iron-containing phases. Simultaneously, no Fe was detected in the reduction products. The atmosphere during the experiment consisted of H_2, CO, CO_2, H_2O, and N_2, with H_2O being generated from both the reduction of SFCA by H_2 and the water–gas shift reaction. The specific reaction for the water–gas shift reaction is as follows:

$$CO_2 + H_2 = CO + H_2O \quad (2)$$

Consequently, the FactSage thermodynamic software was employed in this study to calculate the equilibrium gas-phase composition of the water–gas shift reaction under different atmospheric conditions listed in Table 1, where N_2 served as a protective gas and did not participate in the reaction. Figures 7a, 8a and 9a illustrate the variation curves of H_2, CO, CO_2, and H_2O content (%) as a function of temperature when the H_2 volume fraction is 6%, 10%, and 14%, respectively, at equilibrium. The figures reveal consistent trends in gas content across the three atmospheric conditions. As the temperature increases from 1073 K to 1273 K, the H_2 and CO_2 contents gradually decrease, while the H_2O and CO contents gradually increase. This indicates that the extent of the water–gas shift reaction increases with temperature, leading to changes in the atmospheric composition. Figures 7b, 8b and 9b depict the variation curves of $H_2/(H_2 + H_2O)$ and $CO/(CO + CO_2)$ (%) as a function of temperature when the H_2 volume fraction is 6%, 10%, and 14%, respectively, at equilibrium. These curves align with the ordinate of the equilibrium phase diagram for the reduction of iron oxides by CO and H_2. Therefore, in conjunction with Figures 7c, 8c and 9c, it can be inferred that, when the reaction reaches equilibrium, it cor-

responds to the stable region of FeO. Within this region, the atmospheric and temperature conditions are not met for the further reduction of FeO to Fe, thus FeO will not undergo further reduction.

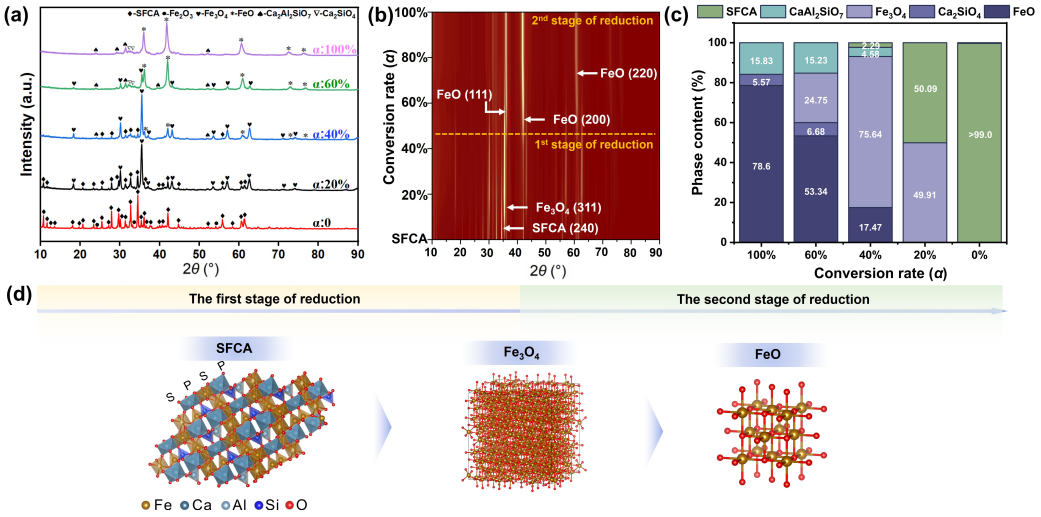

Figure 6. (**a**) XRD patterns of SFCA at different conversion rates. (**b**) Kinetic analysis of XRD pattern. (**c**) Phase content changes during SFCA reduction. (**d**) Schematic diagram of crystal structure transformation during SFCA reduction.

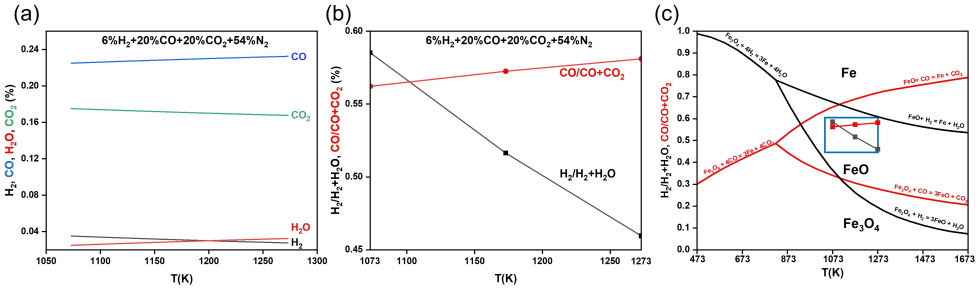

Figure 7. (**a**) Content variation curves (%) of H_2, CO, CO_2, and H_2O at 6% H_2 concentration. (**b**) Content variation curves (%) of $H_2/(H_2 + H_2O)$ and $CO/(CO + CO_2)$ (%) at 6% H_2 concentration. (**c**) Equilibrium phase diagram for the reduction of iron oxides by CO and H_2.

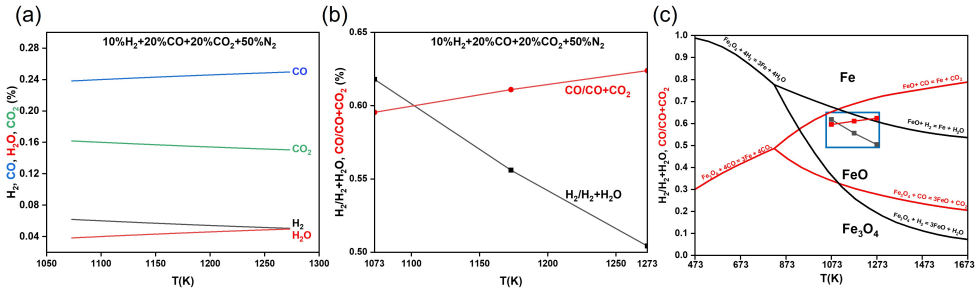

Figure 8. (**a**) Content variation curves (%) of H_2, CO, CO_2, and H_2O at 10% H_2 concentration. (**b**) Content variation curves (%) of $H_2/(H_2 + H_2O)$ and $CO/(CO + CO_2)$ (%) at 10% H_2 concentration. (**c**) Equilibrium phase diagram for the reduction of iron oxides by CO and H_2.

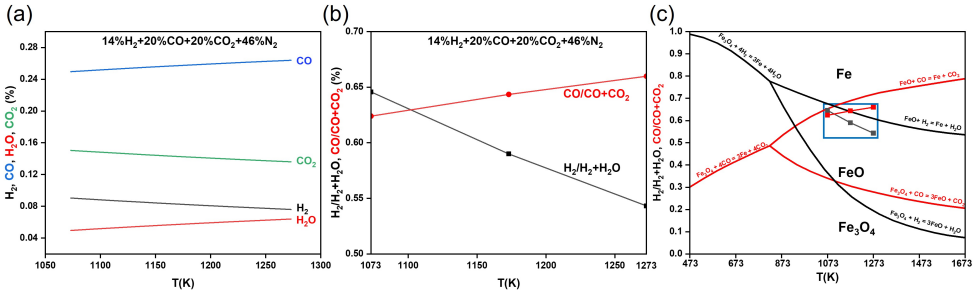

Figure 9. (**a**) Content variation curves (%) of H_2, CO, CO_2, and H_2O at 14% H_2 concentration. (**b**) Content variation curves (%) of $H_2/(H_2 + H_2O)$ and $CO/(CO + CO_2)$ (%) at 14% H2 concentration. (**c**) Equilibrium phase diagram for the reduction of iron oxides by CO and H_2.

3.2.2. SEM-EDS Analysis of SFCA in the Reduction Process

To investigate the microstructural morphology and compositional changes SFCA during the reduction process, SEM-EDS analysis was conducted on SFCA samples with conversion rates of 20%, 40%, 60%, and 100%. The SEM results are presented in Figure 10, and the EDS results are summarized in Table 2. When the conversion rate is 20%, two primary phases were observed: a dark gray phase (represented by Point 1) and an intermediate gray phase (represented by Point 2). According to EDS analysis, Point 1 primarily consisted of Fe, Ca, Si, Al, and O with a mass ratio of approximately Fe:Ca:Si:Al:O ≈ 50.90:11.50:2.70:2.60:32.30; Point 2 was mainly composed of Fe and O with a mass ratio of Fe:O ≈ 72.20:27.80. Combined with XRD analysis, the dark gray phase was identified as SFCA, while the intermediate gray phase was Fe_3O_4. At this stage, the reaction occurred on the surface of SFCA, initiating its reduction to Fe_3O_4. At a conversion rate of 40%, EDS analysis revealed that Point 3, primarily consisting of Fe, Ca, Si, Al, and O with a mass ratio of Fe:Ca:Si:Al:O ≈ 52.15:11.64:3.26:3.14:27.94, corresponded to SFCA; Point 4, mainly composed of Fe and O with a mass ratio of Fe:O ≈ 72.50:27.50, represented by Fe_3O_4. As the reduction reaction progressed, the SFCA content decreased, with iron oxides primarily existing as Fe_3O_4. At a conversion rate of 60%, EDS analysis and element distribution indicated that the intermediate gray phase (represented by Point 5) and light gray phase (represented by Point 6) contained only Fe and O, corresponding to Fe_3O_4 and FeO, respectively. With increasing reduction, the reduced product layer became denser and the particle size decreased. The main reaction at this stage was the reduction of Fe_3O_4 to FeO. Upon reaching a conversion rate of 100%, the reduction was complete. The iron oxide in the product layer consisted only of the light gray phase (represented by Point 7), identified as FeO by EDS analysis. The black phase (represented by Point 8), primarily composed of Ca, Si, Al, and O with a mass ratio of Ca:Si:Al:O ≈ 29.20:19.70:10.72:40.88, was identified as $Ca_2Al_2SiO_7$ and Ca_2SiO_4 based on XRD analysis. These compounds were mainly distributed between the product layer and black pores.

Table 2. Mass% of each elements from EDS results of the reduction products of SFCA at 1000 °C.

Figure 6	α	Number	Fe (%)	Ca (%)	Si (%)	Al (%)	O (%)
(a)	20%	1	50.90	11.50	2.700	2.600	32.30
		2	72.20	0	0	0	27.80
(b)	40%	3	52.15	11.64	3.260	3.140	27.94
		4	72.50	0	0	0	27.50
(c)	60%	5	73.30	0	0	0	26.70
		6	76.90	0	0	0	23.10
(d)	100%	7	77.20	0	0	0	22.80
		8	0	29.20	19.70	10.22	40.88

From the SEM images, it can be inferred that Sample D is relatively dense, whereas Sample A is more porous. In the initial stage of the reduction reaction, SFCA begins to

reduce to form Fe_3O_4, with a thin product layer. As the reduction reaction proceeds, the primary reaction shifts to the reduction of Fe_3O_4 to FeO, and the layers of reduced products, Fe_3O_4 and FeO, gradually thicken. In summary, these observations indicate that the reduction reaction of SFCA proceeds progressively from the outside inward. Furthermore, regions with a higher degree of reduction are denser and exhibit smaller particle sizes, while regions with a lower degree of reduction are more porous and display larger particle sizes.

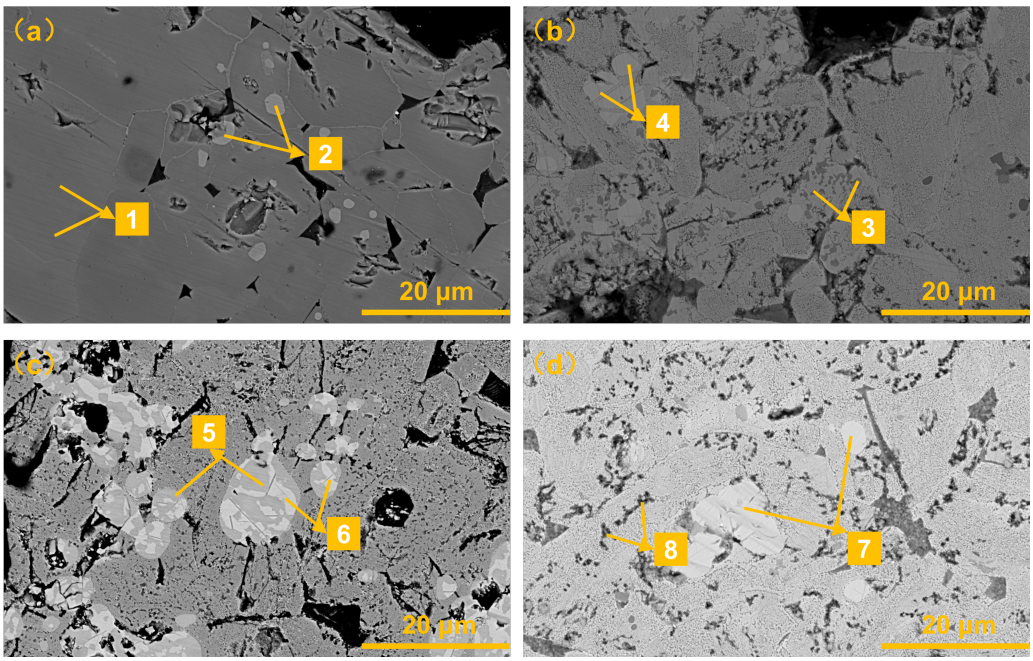

Figure 10. SEM pictures of SFCA at different conversion rates at 1273K: (**a**) 20%, (**b**) 40%, (**c**) 60%, (**d**) 100%.

3.3. Reduction Reaction Dynamic of SCFA

To elucidate the hydrogen-rich reduction process of SFCA more clearly, the influence of temperature and H_2 content on the reduction behavior of SFCA was investigated. The analysis and discussion of the reduction process were conducted using data from isothermal reduction experiments. Figure 11a presents the weight change curves of SFCA over time at various temperatures when the H_2 volume fraction was 6%, while Figure 11b shows the weight change curves of SFCA over time under different H_2 volume fractions at a temperature of 1073 K. It can be observed that as the temperature increases from 1073 K to 1273 K, the reduction process accelerates, with the times to reach phase equilibrium being 88 min, 72 min, and 50 min, respectively. Similarly, at a specific temperature of 1273 K, with the increase in H_2 content, the time for SFCA to reach phase equilibrium gradually decreases to 50 min, 42 min, and 26 min. Since the reduction of SFCA by H_2 and CO is a gas–solid reaction, commonly used kinetic model functions for gas–solid reactions are listed in Table 3 [22–24]. Under isothermal conditions, the kinetic equation for the SFCA reaction can be expressed as [25]:

$$kt = G(\alpha) \tag{3}$$

where $G(\alpha)$ represents the integral form of the reaction mechanism function; k denotes the reaction rate constant; and t stands for time. By performing a linear fit to the $G(\alpha) \sim t$ curve, we can derive the mechanism function $G(\alpha)$ that is appropriate for the reduction process, along with the corresponding model.

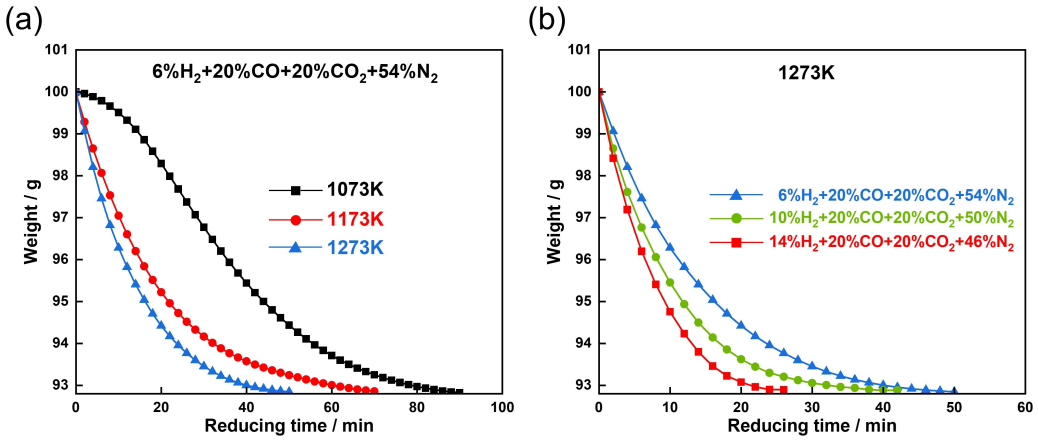

Figure 11. (**a**) Curves of SFCA weight with reduction time at different temperatures. (**b**) Curves of SFCA weight with reduction time at different H_2 volume fractions.

Table 3. Kinetic model function.

Model	$f(\alpha)$	$G(\alpha)$	Reaction Mechanism
Diffusion model	$1/2\alpha$	α^2	1D diffusion
	$-ln(1-\alpha)-1$	$(1-\alpha)ln(1-\alpha)+\alpha$	2D diffusion
	$1.5(1-\alpha)^{2/3}[1-(1-\alpha)^{1/3}]-1$	$[1-(1-\alpha)^{1/3}]^2$	3D diffusion (Jander, n = 2)
	$1.5[(1-\alpha)^{1/3}-1]^{-1}$	$1-2\alpha/3-(1-\alpha)^{2/3}$	3D diffusion (G-B)
Phase boundary Reaction model	$2(1-\alpha)^{1/2}$	$1-(1-\alpha)^{1/2}$	Shrinking core model (n = 2)
	$3(1-\alpha)^{2/3}$	$1-(1-\alpha)^{1/3}$	Shrinking core model (n = 3)

3.3.1. Effect of Temperature on SFCA Reduction Behavior

Figure 12 illustrates the variation curves of SFCA conversion rate and reduction rate over time at temperatures of 1073 K, 1173 K, and 1273 K, with an H_2 volume fraction of 6%. As can be seen from Figure 12a, higher conversion rates achieved at higher temperature at identical reaction times. Additionally, as shown in Figure 12b, the reduction rate curves at elevated temperatures reach a plateau first, indicating that the reduction rate of SFCA increases with rising reduction temperature; thereby, less time is required to reach the end of the reaction. This indicates that an increase in temperature accelerates the reduction process of SFCA. At 1073 K, the reduction rate curve shows an initial increase followed by a decrease. However, at 1173 K and 1273 K, the reduction rate curves exhibit a consistent trend of gradual decrease over time. This phenomenon is primarily attributed to the water–gas shift reaction between CO and H_2 occurring at 1083 K [26]. When the temperature is below 1083 K, the reduction capability of CO surpasses that of H_2; whereas, when the temperature exceeds 1083 K, H_2 exhibits superior reduction capability compared to CO. As the temperature rises, the influence of the water–gas shift reaction on the reduction reaction gradually intensifies, leading to variations in the reduction rate curve.

The relationship curves of $G(\alpha)$ versus t were further calculated for each model listed in Table 3 and subsequently plotted in Figure 13. The fitting was conducted using Equation (2), and the fitting results are presented in Table 4. According to the correlation coefficients (R^2), the reduction process at temperatures of 1073 K, 1173 K, and 1273 K follows the 3D diffusion model (G-B), with the corresponding kinetic mechanism function being $G(\alpha) = 1-2\alpha/3-(1-\alpha)^{2/3}$. This can primarily be attributed to the gradual thickening and densification of the product layers (FeO and Fe_3O_4) formed by the reduction with H_2 and CO as the reduction reaction proceeds, which increases the resistance to diffusion. Therefore, the reduction process is governed by the 3D diffusion model (G-B).

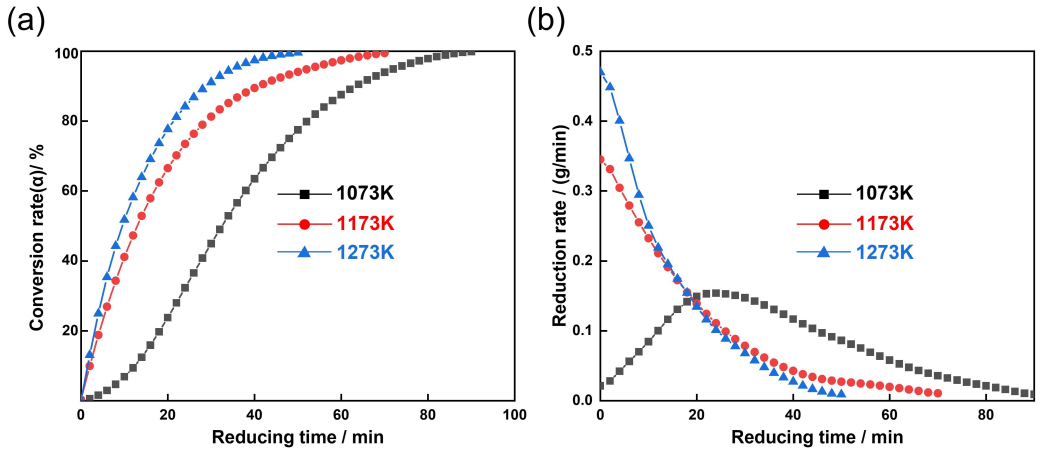

Figure 12. Relationship between (**a**) conversion and reducing time; (**b**) reduction rate and reducing time for different temperatures.

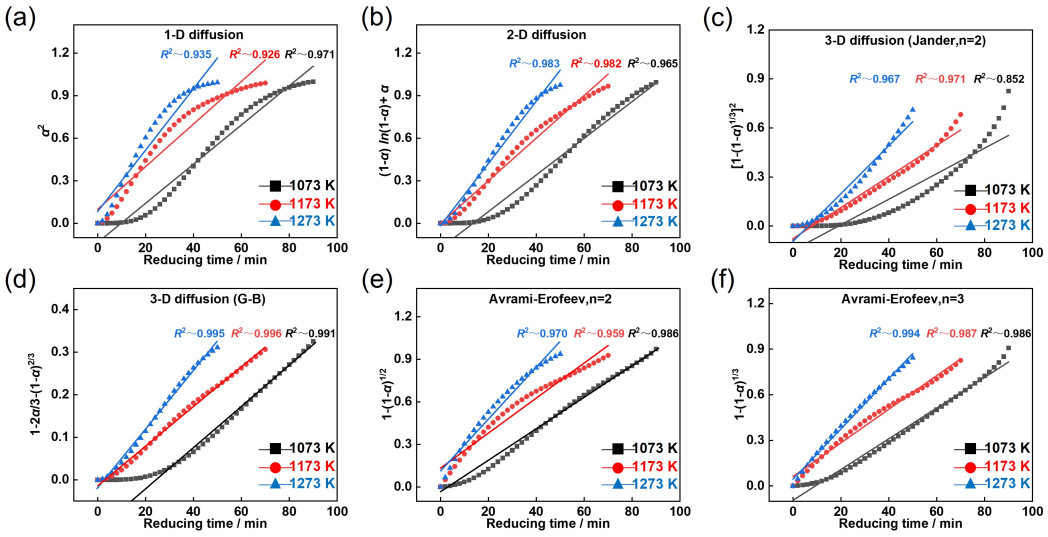

Figure 13. (**a**–**f**) Relationship between $G(\alpha)$ and reduction time t at different temperatures.

Table 4. Fitting results.

$G(\alpha)$	1073 K		1173 K		1273 K	
	k	R^2	k	R^2	k	R^2
α^2	0.014	0.971	0.015	0.926	0.022	0.935
$(1-\alpha)\,ln(1-\alpha)+\alpha$	0.013	0.965	0.015	0.982	0.022	0.983
$[1-(1-\alpha)^{1/3}]^2$	0.008	0.852	0.010	0.971	0.015	0.967
$1-2\alpha/3-(1-\alpha)^{2/3}$	0.004	0.991	0.005	0.996	0.007	0.995
$1-(1-\alpha)^{1/2}$	0.012	0.986	0.012	0.959	0.018	0.970
$1-(1-\alpha)^{1/3}$	0.010	0.986	0.011	0.987	0.017	0.994

The relationship between the rate constant k and the reaction temperature T can be described by the Arrhenius Equation [27]:

$$k = Aexp(-E/RT) \tag{4}$$

where A is the pre-exponential factor; E is the apparent activation energy; and R is the gas constant. Taking the logarithm of both sides of Equation (4) yields:

$$lnk = lnA - "E/RT" \tag{5}$$

By plotting the relationship between lnk and $1000/T$ (Figure 14), the apparent activation energy was determined to be 32.087 kJ·mol^{-1}, with a pre-exponential factor of 0.1419. In summary, under conditions of low H_2 content (6%), the influence of temperature on the reduction process of SFCA follows the 3D diffusion model (G-B). Specifically, as the temperature increases, hydrogen, serving as an active reducing agent, can more effectively diffuse into the pores of the iron ore. Therefore, increasing the reduction temperature is an effective measure to accelerate the SFCA reduction reaction rate. When the reduction temperature reaches the maximum temperature of the lump zone, 1273 K, the reduction rate achieves its fastest.

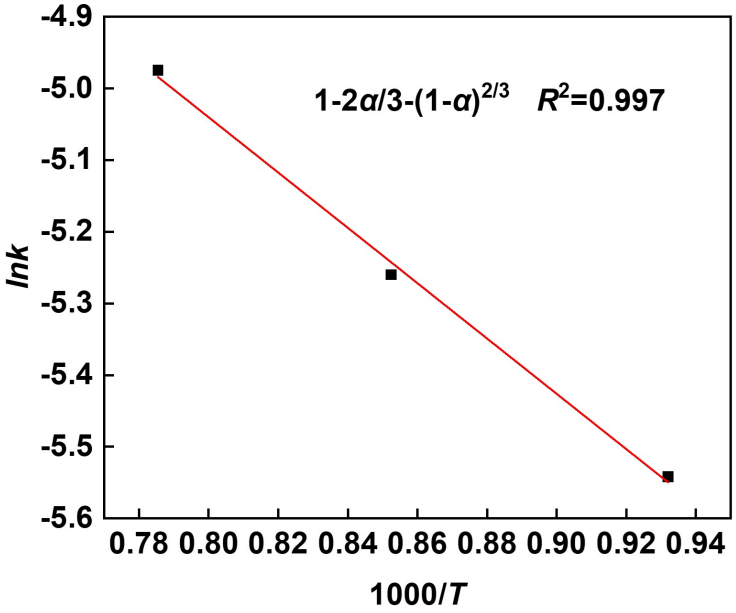

Figure 14. Relationship between lnk and $1000/T$.

3.3.2. Effect of H_2 Content on SFCA Reduction Behavior

Figure 15 presents the conversion rate and reduction rate curves of SFCA as a function of time at temperatures of 1273 K under H_2 volume fractions of 6%, 10%, and 14%. As illustrated, for the same reaction time, the curves with higher H_2 content exhibit greater conversion rates. The reduction rate curves for the three H_2 volume fractions show consistent trends over time: initially, the reduction rate rapidly decreases, exhibiting a linear relationship with time. As the reaction progresses into the mid-to-late stages, the reduction rate begins to change more slowly. Additionally, the reduction rate curve under a 14% H_2 volume fraction is the first to reach a plateau, indicating that increasing the H_2 content can enhance the reaction rate.

As depicted in Figure 16, the $G(\alpha) \sim t$ curves under various models have been further fitted. The fitting outcomes are tabulated in Table 5. At H_2 volume fractions of 6% and 10%, the data align with the 3D diffusion model (G-B), characterized by the kinetic mechanism function $G(\alpha) = 1 - 2\alpha/3 - (1-\alpha)^{1/3}$. When the H_2 volume fraction reaches 14%, the reaction mechanism transitions to the Shrinking core model (n = 3), characterized by the kinetic mechanism function $G(\alpha) = 1 - 2\alpha/3 - (1-\alpha)^{1/3}$. In conclusion, augmenting the H_2 content serves as an effective strategy to enhance the reduction reaction rate of SFCA. As H_2 content increases, the concentration gradient during diffusion also rises, leading to a corresponding enhancement in the diffusion driving force and accelerating the diffusion process. Consequently, the reaction gradually transitions from the 3D diffusion model (G-B) to the Shrinking core model. When the H_2 content reaches 14%, the fastest reduction rate is observed.

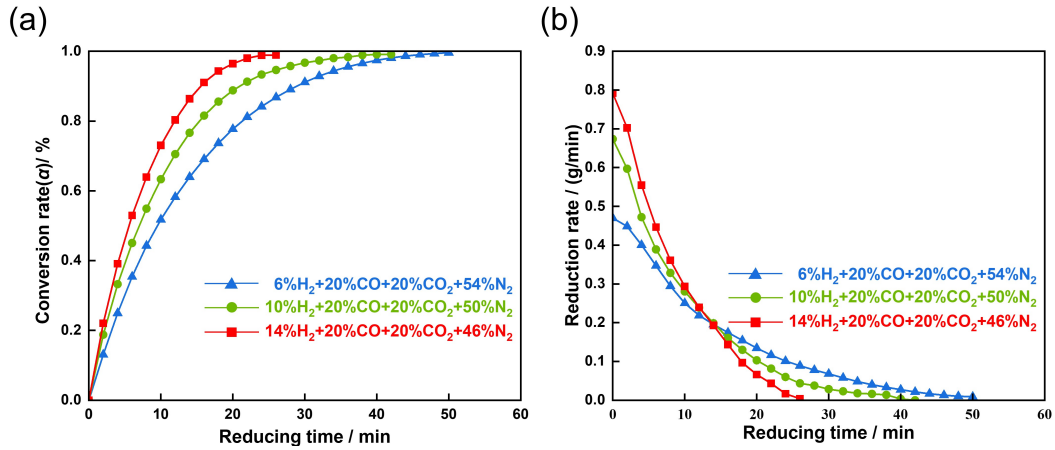

Figure 15. Relationship between (**a**) the conversion and reducing time; (**b**) the reduction rate and the reducing time for different H_2 volume fractions.

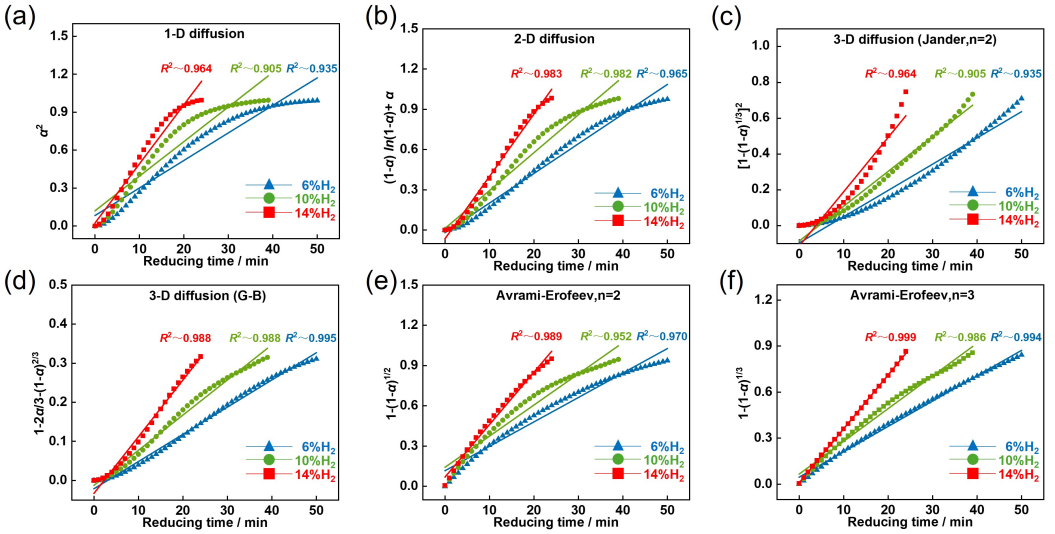

Figure 16. (**a**–**f**) Relationship between $G(\alpha)$ and reduction time t at different H_2 volume fractions.

Table 5. Fitting result.

$G(\alpha)$	6%H_2	10%H_2	14%H_2
	R^2	R^2	R^2
α^2	0.935	0.905	0.964
$(1-\alpha)\,ln(1-\alpha)+\alpha$	0.983	0.966	0.991
$[1-(1-\alpha)^{1/3}]^2$	0.967	0.981	0.929
$1-2\alpha/3-(1-\alpha)^{2/3}$	0.995	0.988	0.988
$1-(1-\alpha)^{1/2}$	0.970	0.952	0.989
$1-(1-\alpha)^{1/3}$	0.994	0.986	0.999

4. Conclusions

This work investigates the hydrogen-rich reduction mechanism of SFCA within the temperature range of the blast furnace's lump zone (1073–1273 K). The research findings are as follows:

(1) Under hydrogen-rich conditions in the blast furnace, with increasing reduction time and conversion rate, SFCA is ultimately reduced to FeO, $Ca_2Al_2SiO_7$, and Ca_2SiO_4. The reduction process of SFCA occurs in two stages: in the first stage, SFCA is reduced to Fe_3O_4 (magnetite); in the second stage, Fe_3O_4 is further reduced to FeO.

(2) Temperature has a significant impact on the reduction process of SFCA. Increasing the temperature accelerates the reduction rate of SFCA, with the fastest rate observed at 1273 K. When the H_2 volume fraction is 6% and the temperatures are 1073 K, 1173 K, and 1273 K, the reduction process of SFCA is governed by the 3D diffusion model (G-B), with an apparent activation energy of 32.087 $kJ \cdot mol^{-1}$ and a pre-exponential factor of 0.1419.

(3) The H_2 content has a notable influence on the reaction rate. As the H_2 content increases, the relative resistance to diffusion gradually decreases, leading to an accelerated reduction rate. The fastest reduction rate is observed when the H_2 volume fraction is 14%. At 1273 K with a H_2 volume fraction of 6%, the reaction follows the 3D diffusion model (G-B); however, when the H_2 volume fractions are 10% and 14%, the reaction mechanism shifts to the Shrinking core model (n = 3).

Author Contributions: Conceptualization, C.H.; Methodology, K.D. and C.H.; Validation, K.D.; Formal analysis, K.D.; Investigation, K.D., C.H., X.S. and G.Y.; Resources, X.S.; Data collation, K.D.; Writing—original draft, K.D.; Writing—review and editing, C.H. and G.Y.; Visualization, G.Y.; Supervision, C.H., X.S. and G.Y.; Project administration, K.D. and C.H.; Funding acquisition, X.S. All authors have read and agreed to the published version of the manuscript.

Funding: This research was funded by China Baowu Low-carbon Metallurgy Innovation Foundation (BWLCF2002122) and Science and Technology Research Project of Colleges and Universities of Hebei Province (ZD2020116).

Data Availability Statement: The data presented in this study are available on request from the corresponding author. The data are not publicly available due to privacy.

Conflicts of Interest: The authors declare no conflicts of interest.

References

1. Bashmakov, I. Greenhouse gas emissions caused by global steel industry: The past, the present and the future. *Ferr. Metall. Bull. Sci. Tech. Econ. Inf.* **2021**, *77*, 882–901. [CrossRef]
2. Holappa, L. A general vision for reduction of energy consumption and CO_2 emissions from the steel industry. *Metals* **2020**, *10*, 1117. [CrossRef]
3. Lopez, G.; Farfan, J.; Breyer, C. Trends in the global steel industry: Evolutionary projections and defossilisation pathways through power-to-steel. *J. Clean. Prod.* **2022**, *375*, 134182. [CrossRef]
4. Lan, C.; Hao, Y.; Shao, J.; Zhang, S.; Liu, R.; Lyu, Q. Effect of H_2 on blast furnace ironmaking: A review. *Metals* **2022**, *12*, 1864. [CrossRef]
5. Gao, X.; Zhang, R.; You, Z.; Yu, W.; Dang, J.; Bai, C. Use of Hydrogen–Rich Gas in Blast Furnace Ironmaking of V–bearing Titanomagnetite: Mass and Energy Balance Calculations. *Materials* **2022**, *15*, 6078. [CrossRef] [PubMed]
6. Pang, Z.; Bu, J.; Yuan, Y.; Zheng, J.; Xue, Q.; Wang, J.; Guo, H.; Zuo, H. The Low-Carbon Production of Iron and Steel Industry Transition Process in China. *Environ. Sci. Technol.* **2024**, *95*, 2300500. [CrossRef]
7. Kleinekorte, J.; Leitl, M.; Zibunas, C.; Bardow, A. What shall we do with steel mill off-gas: Polygeneration systems minimizing greenhouse gas emissions. *Environ. Sci. Technol.* **2022**, *56*, 13294–13304. [CrossRef]
8. Nicol, S.; Chen, J.; Pownceby, M.I.; Webster, N.A. A review of the chemistry, structure and formation conditions of silico-ferrite of calcium and aluminum ('SFCA') phases. *ISIJ Int.* **2018**, *58*, 2157–2172. [CrossRef]
9. Liao, F.; Guo, X.M. Effect of aluminum content on reduction of silico-ferrite of calcium and aluminum (SFCA). *Mater. Res. Express* **2019**, *6*, 106501. [CrossRef]
10. Cho, S.; Kim, S.W.; Jung, S.M. Effects of Adding Iron Ores-based Calcium Ferrites to the Sinter Mix on Sinter Quality and Reduction of CO_2, NO and SO_2. *ISIJ Int.* **2022**, *62*, 2587–2598.
11. Heidari, A.; Niknahad, N.; Iljana, M.; Fabritius, T. A review on the kinetics of iron ore reduction by hydrogen. *Materials* **2021**, *14*, 7540. [CrossRef] [PubMed]
12. Sabat, K.C. Physics and chemistry of solid state direct reduction of iron ore by hydrogen plasma. *Phys. Chem. Solid State* **2021**, *22*, 292–300. [CrossRef]
13. Lan, R.z.; Wang, J.s.; Han, Y.h.; She, X.f.; Wang, L.t.; Qing-guo, X. Reduction behavior of sinter based on top gas recycling-oxygen blast furnace. *J. Iron Steel Res. Int.* **2012**, *19*, 13–19. [CrossRef]
14. Heikkilä, A.; Iljana, M.; Bartusch, H.; Fabritius, T. Reduction of iron ore pellets, sinter, and lump ore under simulated blast furnace conditions. *Steel Res. Int.* **2020**, *91*, 2000047. [CrossRef]
15. Lyu, Q.; Qie, Y.; Liu, X.; Lan, C.; Li, J.; Liu, S. Effect of hydrogen addition on reduction behavior of iron oxides in gas-injection blast furnace. *Thermochim. Acta* **2017**, *648*, 79–90. [CrossRef]

16. Murakami, T.; Kodaira, T.; Kasai, E. Reduction and disintegration behavior of sinter under N_2–CO–CO_2–H_2–H_2O gas at 773 K. *ISIJ Int.* **2015**, *55*, 1181–1187. [CrossRef]
17. Noguchi, D.; Ohno, K.i.; Maeda, T.; Nishioka, K.; Shimizu, M. Effect of CO gas concentration on reduction rate of major mineral phase in sintered iron ore. *ISIJ Int.* **2013**, *53*, 570–575. [CrossRef]
18. Mao, X.; Garg, P.; Hu, X.; Li, Y.; Nag, S.; Kundu, S.; Zhang, J. Kinetic analysis of iron ore powder reaction with hydrogen—carbon monoxide. *Int. J. Miner. Metall. Mater.* **2022**, *29*, 1882–1890. [CrossRef]
19. Schurmann, E.; Kraume, G. Phase Diagram of $CaO-Fe_2O_3$ in Equilibrium With Air. *Arch. Eisenhuttenwes.* **1976**, *47*, 267–269.
20. Xuan, S.; Lv, X.; Ding, C.; Tang, K.; Li, G.; Pei, G.; Wu, S. Reduction Behavior of Aluminate Calcium Ferrite (CFA) in CO-N_2 Atmosphere. *Steel Res. Int.* **2018**, *89*, 1700452. [CrossRef]
21. Barustan, M.I.A.; Copland, E.; Nguyen, T.B.T.; O'dea, D.; Honeyands, T. Reduction degradation of lump, sinter, and pellets in blast furnace with hydrogen injection. *ISIJ Int.* **2024**, *64*, 1517–1527. [CrossRef]
22. Wiltowski, T.; Hinckley, C.; Smith, G.V.; Nishizawa, T.; Saporoschenko, M.; Shiley, R.; Webster, J. Kinetics and mechanisms of iron sulfide reductions in hydrogen and in carbon monoxide. *J. Solid State Chem.* **1987**, *71*, 95–102. [CrossRef]
23. Zuo, H.b.; Wang, C.; Dong, J.j.; Jiao, K.x.; Xu, R.s. Reduction kinetics of iron oxide pellets with H_2 and CO mixtures. *Int. J. Miner. Metall. Mater.* **2015**, *22*, 688–696. [CrossRef]
24. Hammam, A.; Li, Y.; Nie, H.; Zan, L.; Ding, W.; Ge, Y.; Li, M.; Omran, M.; Yu, Y. Isothermal and non-isothermal reduction behaviors of iron ore compacts in pure hydrogen atmosphere and kinetic analysis. *Min. Metall. Explor.* **2021**, *38*, 81–93. [CrossRef]
25. Lyu, B.; Wang, G.; Yang, F.; Zuo, H.; Xue, Q.; Wang, J. Kinetic analysis of isothermal and non-isothermal reduction of iron ore fines in hydrogen atmosphere. *Metals* **2022**, *12*, 1754. [CrossRef]
26. Chen, Y.; Zuo, H. Review of hydrogen-rich ironmaking technology in blast furnace. *Ironmak. Steelmak.* **2021**, *48*, 749–768. [CrossRef]
27. Xing, L.Y.; Zou, Z.S.; Qu, Y.X.; Shao, L.; Zou, J.Q. Gas–solid reduction behavior of in-flight fine hematite ore particles by hydrogen. *Steel Res. Int.* **2019**, *90*, 1800311. [CrossRef]